

Drag Reduction and Energy Saving by Spanwise Traveling Transversal Surface Waves for Flat Plate Flow

Marian Albers¹ · Pascal S. Meysonnat¹ ·
Daniel Fernex² · Richard Semaan² · Bernd
R. Noack^{3,2,4,5} · Wolfgang Schröder^{1,6}

June 26, 2021

Abstract Wall-resolved large-eddy simulations are performed to study the impact of spanwise traveling transversal surface waves in zero-pressure gradient turbulent boundary layer flow. Eighty variations of wavelength, period, and amplitude of the space- and time-dependent sinusoidal wall motion are considered for a boundary layer at a momentum thickness based Reynolds number of $Re_\theta = 1000$. The results show a strong decrease of friction drag of up to 26 % and considerable net power saving of up to 10 %. However, the highest net power saving does not occur at the maximum drag reduction. The drag reduction is modeled as a function of the actuation parameters by support vector regression using the LES data. A substantial attenuation of the near-wall turbulence intensity and especially a weakening of the near-wall velocity streaks are observed. Similarities between the current actuation technique and the method of a spanwise oscillating wall without any normal surface deflection are reported. In particular, the generation of a directional spanwise oscillating Stokes layer is found to be related to skin-friction reduction.

Keywords Turbulent Boundary Layer, Drag Reduction, Transversal Traveling Surface Wave, Large-Eddy Simulation, Active Flow Control

Marian Albers
E-mail: m.albers@aia.rwth-aachen.de

¹ Institute of Aerodynamics, RWTH Aachen University, Wüllnerstrasse 5a, 52062 Aachen, Germany

² Institut für Strömungsmechanik, Technische Universität Braunschweig, Hermann-Blenk-Str. 37, 38108 Braunschweig, Germany

³ LIMSI, CNRS, Université Paris-Saclay, Bât 507, rue du Belvédère, Campus Universitaire, F-91403 Orsay, France

⁴ Institut für Strömungsmechanik und Technische Akustik (ISTA), Technische Universität Berlin, Müller-Breslau-Straße 8, 10623 Berlin, Germany

⁵ Institute for Turbulence-Noise-Vibration Interaction and Control, Harbin Institute of Technology, Shenzhen Campus, China

⁶ JARA Center for Simulation and Data Science, RWTH Aachen University, Seffenter Weg 23, 52074 Aachen, Germany

1 Introduction

Surface friction in turbulent wall-bounded flows is one of the major contributors to the overall drag of flow over slender bodies in general and passenger planes at cruise flight in particular. Lowering turbulent friction drag is therefore essential to meet future CO₂ reduction goals. Besides preventing fully turbulent flow and benefiting from the considerably lower laminar drag [45], there is substantial past and ongoing research in the field of turbulent drag reduction. Unlike active techniques, which require energy introduction to the system, passive techniques such as riblets [50, 4, 51, 15, 14] and compliant surfaces [7, 23, 31, 53] yield reduced skin friction without any added energy. However, compared to passive approaches, which are optimized for single operating conditions, active techniques are adaptive and, at least for some techniques, can achieve higher net power saving. These results, however, hold mostly in canonical flow setups like turbulent channel flows under laboratory conditions, i.e., at extremely low technology readiness levels.

In the following, we briefly review active flow control techniques that are most relevant to the current study. Particularly, we focus on methods that use either in-plane wall motion, such as forcing parallel to the wall or out of plane wall motion. In this study, we employ actuation that belongs to the latter category. We discuss its similarities and peculiarities over existing techniques, and present its drag reduction and net power saving potentials, which reach 26% and 10% compared to the unactuated flow.

Inspired by turbulence suppression by temporary pressure gradient variations [35], Jung et al. [22] performed the first simulations of spanwise wall oscillations which resulted in significantly lowered friction drag. The method was subsequently investigated in detail in the following years for Poiseuille flow [6, 38] and turbulent boundary layer flow [41, 52, 29]. Detailed analyses indicated an interaction of the oscillating spanwise shear with the near-wall velocity streaks [49, 1]. Furthermore, it was found that the maximum drag reduction in turbulent boundary layer flow is moderately lower than in turbulent channel flow and is reached at a significantly lower oscillation period [29]. Motivated by this simple but effective approach, other forms of spatio-temporal forcing have been developed, which is excellently discussed by Quadrio [37]. A modified variant of the purely temporal oscillations of spanwise velocity [49] are spanwise traveling waves of spanwise forcing [10, 11] or spanwise traveling waves of a flexible surface [54]. Although the techniques are different in their actuation principle, the effect of introducing oscillating spanwise shear close to the wall is alike.

Another actuation variant is spanwise traveling transversal surface waves [20]. Instead of directly introducing spanwise velocity, the surface is wavyly deflected in the wall-normal direction to generate a secondary flow field of periodic wall-normal and spanwise fluctuations. Positive drag reduction using this technique was achieved experimentally [20, 47, 30] and numerically for channel flow [48], boundary layer flow [26, 28, 27, 19], and airfoil flow [2]. Tomiyama and Fukagata [48] observed a possible shielding effect of quasi-streamwise vortices from the wall by the wave-like deformations and showed that a combination of the thickness of the Stokes layer, i.e., the actuation period, and the actuation velocity amplitudes scales reasonably well with drag reduction.

However, the question remains what happens at higher amplitudes and wavelengths and lower periods, especially considering the vast gap between the mostly

relatively short wavelength setups in numerical simulations and the large wavelengths in all experimental setups limited by mechanical actuator constraints. We will investigate if the trend of higher drag reduction for longer wavelengths [11] can be confirmed. Furthermore, an optimum forcing period T^+ in inner scaling was not determined for this technique and it remains an open question if one exists and if so if it is in the range of other techniques, e.g., $T^+ \approx 70$ for spanwise oscillating wall in turbulent boundary layer flow [29]. In this study, we address these questions. We investigate the higher reduction trends with longer wavelengths and examine the flow sensitivities over the space spanned by the three actuation parameters, i.e., wavelength, wave period, and wave amplitude, using high-resolution large-eddy simulations (LES) of turbulent boundary layer flow. In total, 80 configurations are computed. The objective is to achieve drag reduction and net energy saving in the range of other actuation techniques and to compare the flow response to that from pure spanwise oscillations.

The paper has the following structure. First, the numerical method is concisely described in section 2. Then the flow setup and all flow and actuation parameters are specified in section 3. The results are discussed in section 4. Finally, the essential results are summarized in section 5.

2 Numerical method

The actuated turbulent boundary layer flow is computed by solving the unsteady compressible Navier-Stokes equations by a large-eddy simulation (LES) formulation. To capture the temporal variation of the geometry, the equations are written in the Arbitrary Lagrangian-Eulerian (ALE) formulation [17] such that the actuated wall can be represented by an appropriate mesh deformation. Additional volume fluxes are determined to satisfy the Geometry Conservation Law (GCL).

The discrete solution is based on a finite-volume approximation on a structured body-fitted mesh. A second-order accurate formulation of the inviscid fluxes using the advection upstream splitting method (AUSM) is applied. The cell-surface values of the flow quantities are reconstructed from the surrounding cell-center values using a Monotone Upstream Scheme for Conservation Laws (MUSCL) type strategy. The viscous fluxes are discretized by a modified cell-vertex scheme at second-order accuracy. The time integration is performed by a second-order accurate five-stage Runge-Kutta scheme, rendering the overall discretization second-order accurate.

The subgrid scales in the LES are implicitly modeled following the monotonically integrated large-eddy simulation approach [5], i.e., the numerical dissipation of the AUSM scheme models for the viscous dissipation of the high wavenumber turbulence spectrum [33]. Thus, the small-scale structures are not explicitly resolved in the whole flow domain and the grid is used as a spatial filter resolving the large energy-containing structures in the inertial subrange.

The numerical method has thoroughly been validated by computing a wide variety of internal and external flow problems [43, 3, 39, 46]. Analyses of drag reduction have been performed for riblet structured surfaces [24] and for traveling transversal surface waves in canonical turbulent boundary layer flow [26, 27, 28, 34] and in turbulent airfoil flow [2]. The quality of the results confirms the validity of the approach for the current flow problem.

3 Computational Setup

The zero-pressure gradient (ZPG) turbulent boundary layer flow over a wall actuated by a sinusoidal wave motion is defined in a Cartesian domain with the x -axis in the main flow direction, the y -axis in the wall-normal direction, and the z -axis in the spanwise direction. The velocity vector in the Cartesian frame of reference $\mathbf{x} = (x, y, z)$ is denoted by $\mathbf{u} = (u, v, w)$, the pressure is given by p , and the density by ρ . The flow variables are non-dimensionalized using the flow quantities at rest, the speed of sound a_0 , and the momentum thickness of the boundary layer at $x_0 = 0$ such that $\theta(x_0 = 0) = 1$. The momentum thickness based Reynolds number is $Re_\theta = u_\infty \theta / \nu = 1,000$ at x_0 where u_∞ is the freestream velocity and ν is the kinematic viscosity. The Mach number is $M = 0.1$, i.e., the flow is nearly incompressible. Note that unlike standard ZPG turbulent boundary layer flow, the actuated flow is statistically three-dimensional due to the wave propagating in the z -direction.

An overview of the setup is given in Fig. 1. The dimensions of the physical domain are $L_x = 190 \theta$, $L_y = 105 \theta$ in the streamwise and wall-normal direction. For the spanwise direction, five domain widths, $L_z \in [21.65 \theta, 25.98 \theta, 34.64 \theta, 38.97 \theta, 64.95 \theta]$ are used. The mesh resolution is $\Delta x^+ = 12.0$ in the streamwise direction, $\Delta y^+|_{\text{wall}} = 1.0$ in the wall-normal direction with gradual coarsening off the wall up to $\Delta y^+ = 16.0$ at the boundary layer edge, and $\Delta z^+ = 4.0$ in the spanwise direction. This yields a DNS-like resolution near the wall. Away from the wall, the resolution requirements are lower such that overall an LES resolution is achieved.

At the inflow of the domain, the reformulated synthetic turbulence generation (RSTG) method by Roidl et al. [42] is used to prescribe a fully turbulent inflow distribution with an adaptation length of less than five boundary-layer thicknesses δ_{99} . A fully turbulent boundary layer is achieved at x_0 , which marks the onset of the actuation. Characteristic outflow conditions are applied at the downstream and upper boundaries, whereas periodic conditions are used in the spanwise direction. On the wall, no-slip conditions are imposed and the wall motion is described by

$$y^+|_{\text{wall}}(z^+, t^+) = g(x)A^+ \cos\left(\frac{2\pi}{\lambda^+}z^+ + \frac{2\pi}{T^+}t^+\right), \quad (1)$$

where $A^+ = Au_\tau/\nu$ is the amplitude, $\lambda^+ = \lambda u_\tau/\nu$ is the wavelength, and $T^+ = Tu_\tau^2/\nu$ is the period. If not otherwise stated an inner scaling is used for all wave parameters, i.e., the quantities are scaled by the kinematic viscosity ν and the friction velocity u_τ of the non-actuated reference case N_1 .

In total, 80 variations of $A^+ \in [0, 78]$, $T^+ \in [20, 120]$, and $\lambda^+ \in [200, 3000]$ are simulated. A detailed list of all parameter combinations can be found in Tab. A1 in the appendix. Note that the narrowest domain has a spanwise extent of $L_z^+ = 1000$ such that for all wavelengths $\lambda^+ < 1000$ multiple wavelengths are considered. A sketch of all wavelengths and the respective maximum amplitude at each wavelength is illustrated in Fig. 2. To enable a smooth spatial transition from the stationary flat plate to the deflected wall and vice versa, the piecewise defined

function

$$g(x) = \begin{cases} 0 & \text{if } x < -5 \\ \frac{1}{2} \left[1 - \cos \left(\frac{\pi(x+5)}{10} \right) \right] & \text{if } -5 \leq x < 5 \\ 1 & \text{if } 5 \leq x < 130 \\ \frac{1}{2} \left[1 + \cos \left(\frac{\pi(x-130)}{10} \right) \right] & \text{if } 130 \leq x < 140 \\ 0 & \text{otherwise} \end{cases} \quad (2a)$$

(2b)

is used in Eq. 1.

The drag is integrated over the wall surface within the streamwise interval $x \in [50.0, 100.0]$ and over the entire spanwise extent. This area is colored in Fig. 1. Hence, the drag is only computed in the region where the flow is fully influenced by the traveling wave actuation. The actuated boundary layer is not impacted by the flow upstream and downstream of the actuated surface.

The computing strategy is such that first, the non-actuated reference case is simulated for $tu_\infty/\theta \approx 650$ convective times until a quasi-steady state is observed in the integrated drag. All actuated cases are then initialized by the flow field of the reference case and the transition from a flat plate to an actuated wall flow is performed via a temporal decay controlled by $1 - \cos(t)$. Once a new quasi-steady state is observed all simulations are averaged over $tu_\infty/\theta \approx 1250$ times.

4 Results

In the following, the results of the parameter study will be investigated in detail. First, a grid convergence study is performed in Sec. 4.1. Then, the wall-shear stress reductions as a function of the wave parameters are thoroughly discussed in Sec. 4.2. The findings are compared with data from the literature for the same and similar drag reduction techniques. This analysis is followed in Sec. 4.3 by a discussion of the variation of the total drag, i.e., the wall-shear stress multiplied by the wetted surface, since the wetted surface changes for different parameter setups. Support vector regression is used to predict drag reductions and to examine the drag reduction sensitivities for varying actuation settings is concisely presented in Sec. 4.4. The statistics of the non-actuated and actuated flow field are compared, and links to drag reduction mechanisms are drawn in Sec. 4.5. The spanwise shear distribution in the near-wall region with special focus on the periodic Stokes shear and its relevance for drag reduction is analyzed in Sec. 4.6. Finally, the net energy balance results are presented in Sec. 4.7.

4.1 Grid convergence

To ensure a sufficient grid resolution for the large-eddy simulation of the actuated turbulent boundary layer flow a grid convergence study is conducted. The data of the three meshes that are compared are listed in Tab. 1. Besides the mesh data, the drag reduction Δc_d , which is defined in Sec. 4.3, is given. The actuation parameters in inner coordinates are $\lambda^+ = 1000$, $T^+ = 40$, and $A^+ = 40$. They define case N_{24} in Tab. A1 in the appendix for which a moderate drag reduction is

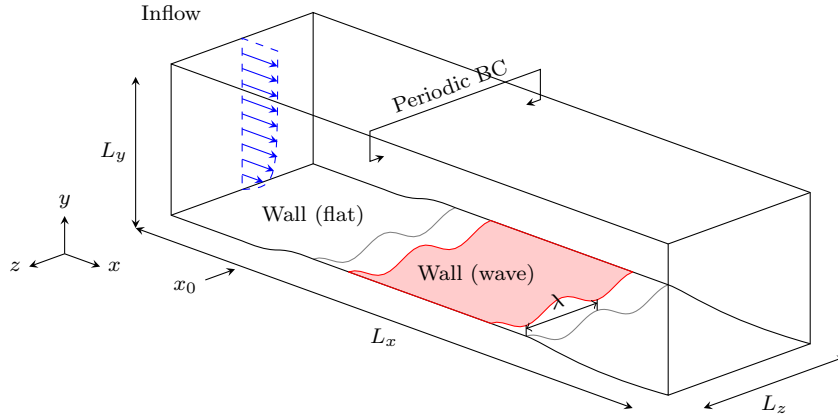


Fig. 1: Overview of the physical domain of the actuated turbulent boundary layer flow. The quantities L_x , L_y , and L_z are the dimensions of the domain in the Cartesian directions, λ is the wavelength of the spanwise traveling wave, and x_0 marks the onset of the actuation. The surface area A_{surf} for the integration of the wall-shear stress τ_w is shaded red.

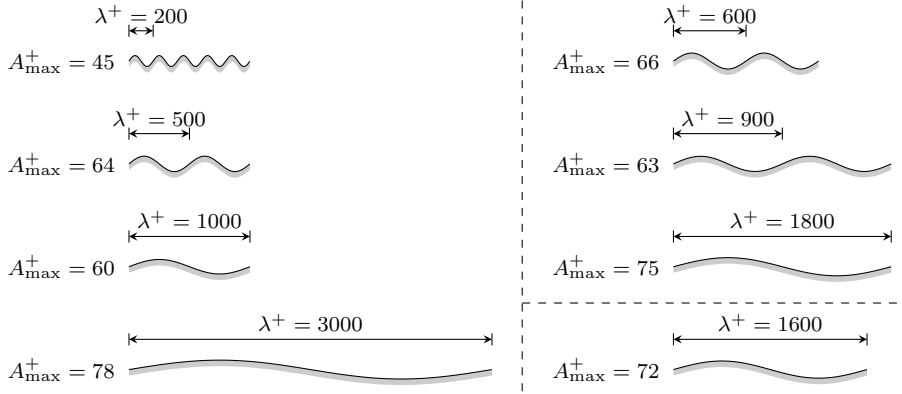


Fig. 2: Overview of the sinusoidal wall function with all used wavelengths and the corresponding maximum amplitude. The spanwise extent is varied to fit an integer number of wavelengths into the domain.

achieved. It is evident from the results in Tab. 1 that the drag reduction values on the standard and the fine grid are nearly identical. On the coarse grid, however, a clear deviation is determined.

A comparison of the symmetric stresses and the shear-stress component of the Reynolds stress tensor at the streamwise location of $x/\theta = 50$, i.e., on the non-actuated surface at $Re_\theta = 1033$, is shown in Fig. 3. The distributions of the standard and the fine mesh nearly collapse for the non-actuated reference case and for the actuated case N_{24} for all four components. Note that similar results were determined for other actuation parameter configurations. Only on the coarse mesh larger deviations are obtained. Furthermore, the data of the non-actuated

Case	Δx^+	$\Delta y^+ _{\text{wall}}$	Δz^+	N_{BL}	$N_i \times N_j \times N_k$	N_{total}	Δc_d
coarse	20.0	1.5	8.0	78	$438 \times 118 \times 125$	$6.5 \cdot 10^6$	19.28 %
standard	12.0	1.0	4.0	89	$732 \times 131 \times 250$	$24.0 \cdot 10^6$	15.17 %
fine	10.0	0.7	2.0	100	$877 \times 142 \times 500$	$62.3 \cdot 10^6$	15.18 %

Table 1: Summary of the grid spacings Δx^+ , Δy^+_{wall} , and Δz^+ , the number of cells inside the boundary layer N_{BL} , the number of cells in the coordinate directions, the total number of cells, and the computed drag reduction Δc_d for the coarse, standard, and fine grid.

reference case for the standard and the fine mesh shows good agreement with DNS data [44] of a turbulent boundary layer at a similar Reynolds number, i.e., $Re_\theta = 1006$.

In conclusion, the analysis of the data shows that the resolution of the standard grid can be considered sufficient to accurately predict actuated turbulent boundary layer flow.

4.2 Wall-shear stress reductions

The skin-friction reduction Δc_f is defined in percent by

$$\Delta c_f = \frac{\tau_{w,\text{ref}} - \tau_{w,\text{act}}}{\tau_{w,\text{ref}}} \cdot 100,$$

where the wall-shear stress τ_w is averaged over the shaded surface A_{surf} in Fig. 1. The values for Δc_f of the 80 cases are listed in Tab. A1 in the appendix. The dependence of Δc_f on the various parameters, i.e., the wavelength, period, amplitude, and amplitude velocity, is summarized in Fig. 4. The highlighted and numbered distributions are mainly from cases of the upper envelope of the wall-shear stress reduction, i.e., the maximum Δc_f values for the wavelength, the period, and the amplitude are emphasized. The discussion and illustration in Fig. 4 summarize the pronounced varying dependence of the wall-shear stress on the different actuation parameters.

In Fig. 4(a) a quasi-linear increase of the skin-friction reduction Δc_f as a function of the wavelength λ^+ is observed. Note, however, that this quasi-linear distribution is achieved by changing simultaneously the amplitude A^+ and the period T^+ . Especially the latter has to undergo quite a non-linear variation to obtain such an approximately linear Δc_f growth.

The dependence of Δc_f on the wave period T^+ at various A^+ and λ^+ is presented in Fig. 4(b). Due to the coupling between the forcing strength and the actuation period, which is in contrast to other actuation methods like spanwise traveling waves of spanwise forcing [11] and traveling waves of flexible wall [54], the optimum period T^+ is determined by an internal, i.e., fluid mechanical, and an external, i.e., actuator, related condition. The ideal T^+ is defined by the streak formation time scale [49], i.e., for oscillatory spanwise forcing the period must be small enough to disrupt the reorganization of the streaks, and a sufficient strength of the forcing, which increases with decreasing period, is required. The dependence of the skin-friction reduction on the period in Fig. 4(b) shows that the optimum

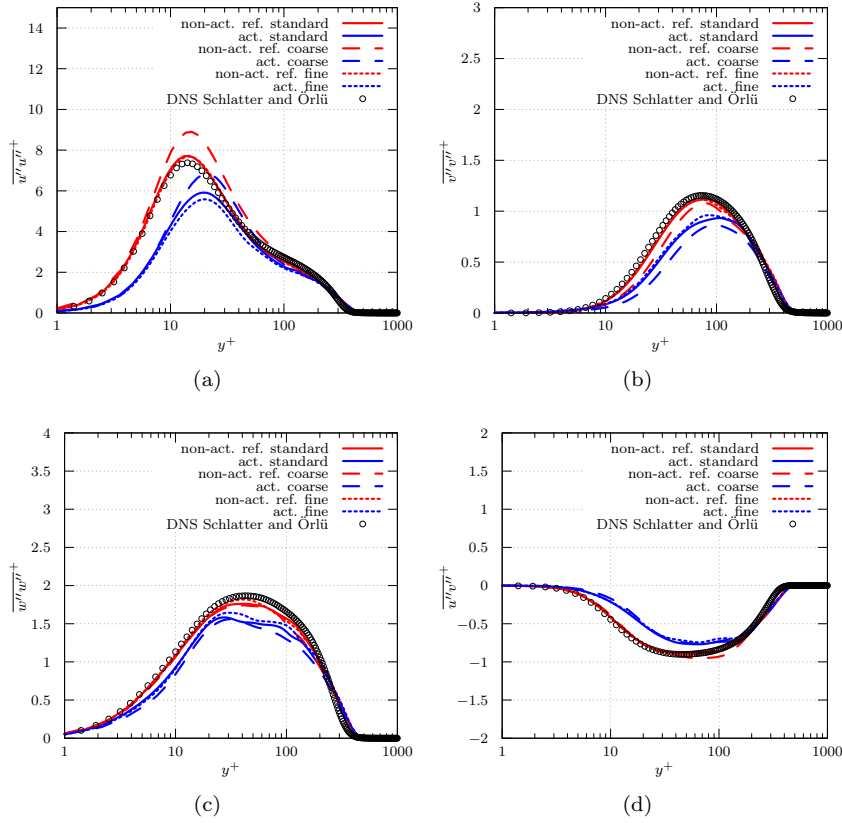


Fig. 3: Comparison of the wall-normal distributions of the symmetric stresses and the shear-stress component of the Reynolds stress tensor on the coarse, standard, and fine grids for the non-actuated reference case and the actuated case N_{24} with DNS data [44].

period among all 80 cases is on the order of $T^+ = \mathcal{O}(50)$, which is slightly lower than the optimum period $T^+ \approx 70$ of a spanwise oscillating wall in turbulent boundary layer flow [29].

Note that likewise tendencies can be found for spanwise traveling oscillatory forcing [11] such as increased drag reduction with higher wavelengths (cf. Fig.4(a)). The longest wavelength considered in this study ($\lambda^+ = 3000$) is comparable to that used in the experimental setups by Tamano and Itoh [47] and Li et al. [30]. Although their lowest investigated period is $T^+ \approx 110$ and thus considerably higher than the optimum found in this study, their results corroborate the tendency of higher wall-shear stress reduction at lower periods in the regime $110 \leq T^+ \leq 302.5$.

The distribution of the skin-friction decrease as a function of the amplitude in Fig. 4(c) shows that the maximum skin-friction reduction is directly coupled to the amplitude. This is to some extent expected since the velocity and thus, the strength

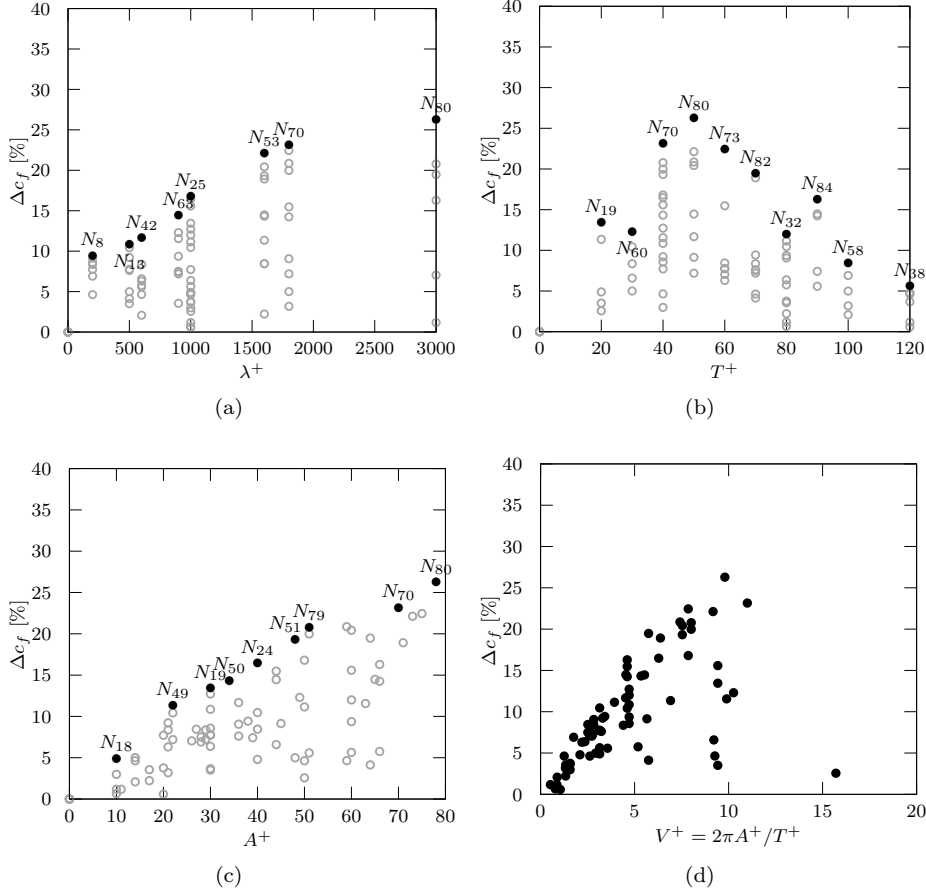


Fig. 4: Dependence of the skin-friction reduction Δc_f on (a) the wavelength λ^+ , (b) the period T^+ , (c) the amplitude A^+ , and (d) the actuation velocity $V^+ = 2\pi A^+/T^+$. For clarity, only the cases that define the upper envelope of the skin-friction reduction Δc_f are shown in (a), (b), and (c).

of the actuation $V^+ = 2\pi A^+/T^+$ is directly related to the amplitude. That is, at a given period the strength of the actuation is determined by the amplitude. This is confirmed by the experimental findings of Li et al. [30]. They obtain in a lower amplitude range a monotonic increase of the skin-friction reduction for increasing amplitude. Figure 4(d) presents the skin-friction reductions as a function of the velocity amplitude of the actuation V^+ , where the scaling shows a quasi-linear behavior for larger wavelengths $\lambda^+ > 1000$.

A similar scaling for Δc_f was proposed by Tomiyama and Fukagata [48] by combining the amplitude of the actuation velocity V^+ (cf. Fig. 4(d)) and the thickness of the Stokes layer $\sqrt{T^+}/(2\pi)$ such that $\Delta c_f = f(A^+ \sqrt{2\pi}/T^+)$ which is plotted in Fig. 5. For shorter wavelengths (cf. Fig. 5(a)), i.e., $\lambda^+ \leq 1000$, a

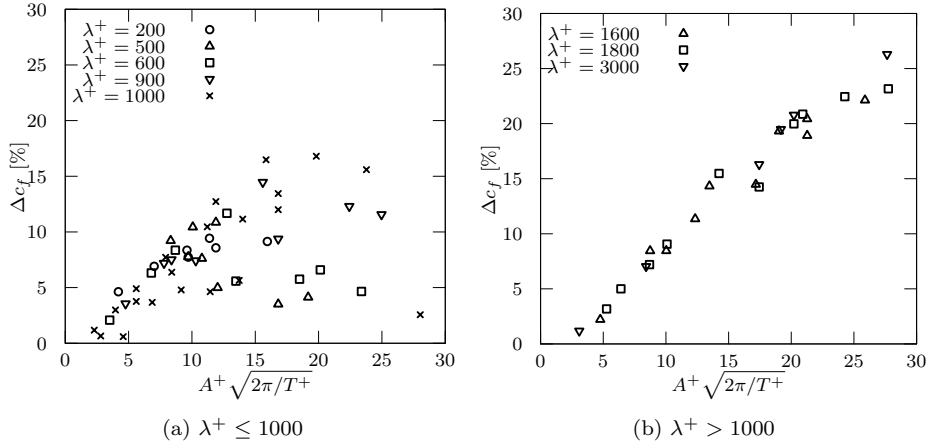


Fig. 5: Relative skin-friction reduction of all cases as a function of the scaling parameter $A^+ \sqrt{2\pi/T^+}$ for (a) $\lambda^+ \leq 1000$ and (b) $\lambda^+ > 1000$.

linear scaling is only observed for small values $A^+ \sqrt{2\pi/T^+} < 10$. Note that the current overall reductions are lower than those in [48] which is likely due to the higher Reynolds number in this study ($Re_\tau = 360$ vs. $Re_\tau = 180$ in [48]) and due to a generally lower skin-friction reduction efficiency in turbulent boundary layers compared to turbulent channel flow [40]. For higher scaling factor values, the distribution is more scattered. For larger wavelengths $\lambda^+ > 1000$ (cf. Fig. 5(b)), the skin-friction reduction scales almost linearly over the entire range. Above a certain value $A^+ \sqrt{2\pi/T^+} \gtrsim 20$, however, the linear behavior of the skin-friction reduction deteriorates. We believe the reason for this degradation is the large momentum injection into the boundary layer via too high a velocity amplitude. This increases the spanwise velocity component which leads to an amplified turbulent exchange.

4.3 Drag reduction

Introducing a wave motion of the surface means that the area of the moving wall increases with the amplitude and the wavelength of the wave. The data in Tab. A1 in the appendix shows that this change of the wetted surface ΔA_{surf} can be quite substantial, especially at small wavelengths and high amplitudes. At high wavelengths, this variation becomes rather small. Since the friction drag is defined by the product of the wall-shear stress and the surface interacting with the fluid, the variation of the wetted surface has to be taken into account leading to a non-linear relation between wall-shear stress and friction drag reduction.

The averaged drag reduction is defined as

$$\Delta c_d = \frac{c_{d,\text{ref}} - c_{d,\text{act}}}{c_{d,\text{ref}}} \cdot 100$$

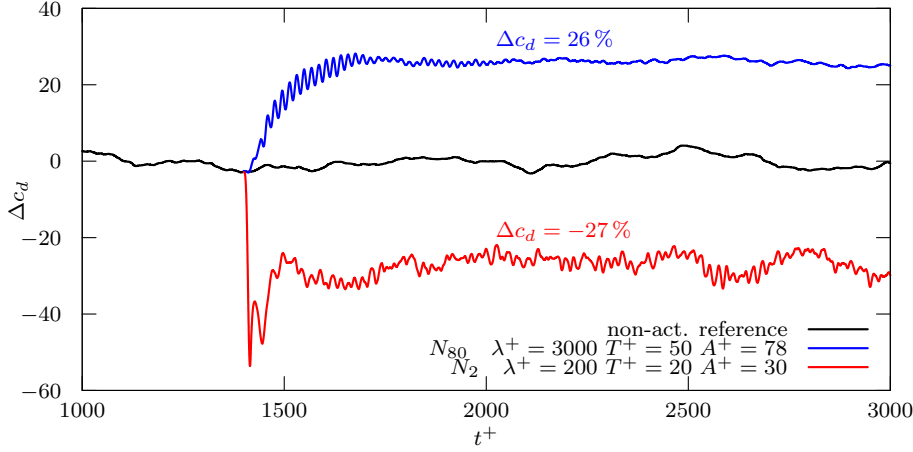


Fig. 6: Temporal evolution of the instantaneous drag reduction Δc_d for the non-actuated reference case, the actuated case with the highest drag reduction (N_{80} , Tab. A1 in the appendix), and the actuated case with the highest drag increase (N_2 , Tab. A1 in the appendix).

where c_d is the drag coefficient computed by an integration over the shaded surface A_{surf} in Fig. 1,

$$c_d = \frac{2}{\rho_\infty u_\infty^2 A_{\text{ref}}} \int_{A_{\text{surf}}} \tau_w \mathbf{e}_y \cdot \mathbf{n} dA .$$

The quantity \mathbf{n} denotes the unit normal vector of the surface, \mathbf{e}_y is the unit vector in the y -direction, and $A_{\text{ref}} = 1$ is the reference surface.

The data in Tab. A1 in the appendix evidences the differences between Δc_f and Δc_d , especially at small wavelengths. The highest drag reduction is $\Delta c_d = 26\%$ for a wavelength of $\lambda^+ = 3000$, a period of $T^+ = 50$, and an amplitude of $A^+ = 78$. Due to the large wavelength, the increase of the wetted surface is only $\Delta A_{\text{surf}} = 0.7\%$. The highest drag increase $\Delta c_d = -27\%$ with the highest corresponding skin-friction coefficient increase $\Delta c_f = -7\%$ is observed for $\lambda^+ = 200$, $T^+ = 20$, and $A^+ = 30$. As stated before, this configuration with a small wavelength suffers considerably from a drastic increase of the wetted surface $\Delta A_{\text{surf}} = 19.4\%$.

The temporal distributions of the instantaneous drag of the "best" and "worst", i.e., highest and lowest drag reduction N_{80} $\Delta c_d = 26\%$ and N_2 $\Delta c_d = -27\%$, which is a massive drag increase, are compared exemplarily in Fig. 6, with the instantaneous drag of the reference case. The temporal fluctuations of the drag appear stronger for the "worst" case. Note that due to the larger wavelength the drag of the "best" case is numerically integrated over a three times larger spanwise extent. Due to the spanwise averaging, this leads to the temporally smoother distribution of the N_{80} ($\Delta c_d = 26\%$) case compared to the N_2 ($\Delta c_d = -27\%$) case.

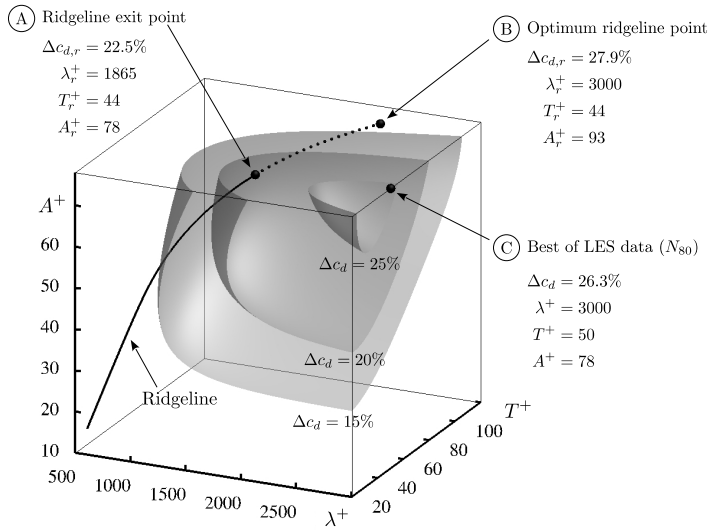


Fig. 7: Actuation response surface. The gray surfaces represent drag reduction at three levels: $\Delta c_d = 15, 20,$ and 25% . The thick black line illustrates the ridgeline. Its solid portion is interpolated using all LES data. The dotted ridgeline between points A and B extrapolates a better actuation response at given λ^+ for amplitudes $A^+ > 78$, i.e. beyond the investigated parameter range. Point C corresponds to the actuation parameters of the LES simulation N_{80} with the largest drag reduction.

4.4 Drag reduction modeling and sensitivity analysis

In the following, the drag reduction Δc_d is modeled as a function of the actuation parameters λ^+ , T^+ , and A^+ . For this task, LES simulations provide only a sparse data set comprising 80 points. This amount would roughly correspond to a Cartesian discretization of a three-dimensional data space with only $3 \times 3 \times 3$ points. However, the modeling is further complicated by the fact that these points are far from regularly distributed. A dense coverage of the actuation space using expensive LES simulations is hardly feasible.

The modeling is performed using a powerful regression solver from machine learning: support vector regression (SVR) [9]. The algorithm is chosen for its prediction accuracy and its smooth response distribution. SVR is a supervised learning algorithm that constructs a mapping between features or inputs and a known response. Here, SVR maps the actuation parameters λ^+ , T^+ , and A^+ on the averaged drag reduction Δc_d . Note that due to the highly non-linear response behavior and the scarcity of data points at very low wavelengths, cases with wavelengths $\lambda^+ < 500$ are ignored during the modeling process. This range is also of little interest as the best drag reduction is found at larger wavelengths. This data exclusion effectively yields 71 data points instead of 80. Overfitting is prevented with a 5-fold cross-validation. The SVR model has a coefficient of determination of $R^2 = 0.93$ indicating an excellent prediction accuracy.

The SVR model from the LES data is employed to visualize a continuous actuation response in the investigated parameter range of $A^+ \in [0, 78]$, $T^+ \in [20, 120]$, and $\lambda^+ \in [500, 3000]$. Fig. 7 shows the isosurfaces of three drag reduction levels: $\Delta c_d = 15, 20$, and 25% . Within this parameter range, the best performance of 26.5% is achieved at $\lambda^+ = 3000$, $T^+ = 38$ and $A^+ = 78$, which is slightly higher than the best simulated LES configuration N_{80} with $\Delta c_d = 26.3\%$. This location indicates that better drag reduction could be achieved by increasing amplitude and wavelength.

An extrapolation of better performance outside the investigated parameter range is obtained with a *ridgeline*. In every $\lambda^+ = \text{const}$ plane, the drag reduction Δc_d features a single maximum (A_r^+, T_r^+) with respect to the actuation amplitude A^+ and period T^+ . The curve of (A^+, T^+, λ^+) connecting all these λ^+ -dependent Δc_d maxima is the *ridgeline*, which is illustrated as a thick black curve in Fig. 7. Variables on this ridgeline are denoted by the subscript ‘r’.

In the range $\lambda^+ \in [560, 1865]$, this maximum is inside the modeled T^+ and A^+ data range. It is illustrated by the solid black curve. However, the ridgeline leaves this modeled data range through the exit point A at the top surface $A^+ = 78$ near $\lambda^+ \approx 1865$. The ridgeline is extrapolated outside the data range and depicted as dotted curve between points A and B . The extrapolation method is detailed in [12]. Along the ridgeline, Δc_d monotonously increases from 7% at $\lambda^+ = 560$ to the maximum of 27.9% at $\lambda^+ = 3000$ (point B). Note that this point is outside the current LES parameter range.

The ridgeline defines a ‘skeleton’ of the parametric behavior as illustrated in Fig. 8. Fig. 8a shows its projection in the $\lambda^+ - T^+$ and $\lambda^+ - A^+$ planes. Like in Fig. 7, the dotted sections correspond to the extrapolated ridgeline between points A to B . The amplitude A_r^+ and period T_r^+ along the ridgeline monotonously increase with the wavelength λ^+ . The period asymptotes rapidly towards 44 . The amplitude continually increases with the wavelength although at a decreasing rate.

An intriguing physical insight about the drag-reduction mechanism is revealed in Fig. 8b complementing Fig. 5b. The relative drag reduction Δc_d along the ridgeline is shown as a function of the scaling parameter proposed by Tomiyama and Fukagata [48] based on a Stokes layer of a transverse wall oscillation. Δc_d clearly exhibits a linear behavior along the ridgeline in the scaling parameter range between 15 and 30 . Away from the ridgeline, the scaling shows scatter on the order of that observed in Fig. 5(b).

4.5 Turbulent flow statistics

In the following, the mean statistics of a drag reduced flow will be investigated in detail. For this analysis, the case with the highest drag reduction, i.e., the case N_{80} , will be considered. If data from other cases is used, it is explicitly indicated. All presented wall-normal distributions are considered at the streamwise position $x = 90\theta$, which is located in the actuated region. The actuated fully developed turbulent flow possesses a momentum based Reynolds number $\text{Re}_\theta = 1077$. The flow field of the actuated cases is phase averaged in the spanwise direction. Therefore,

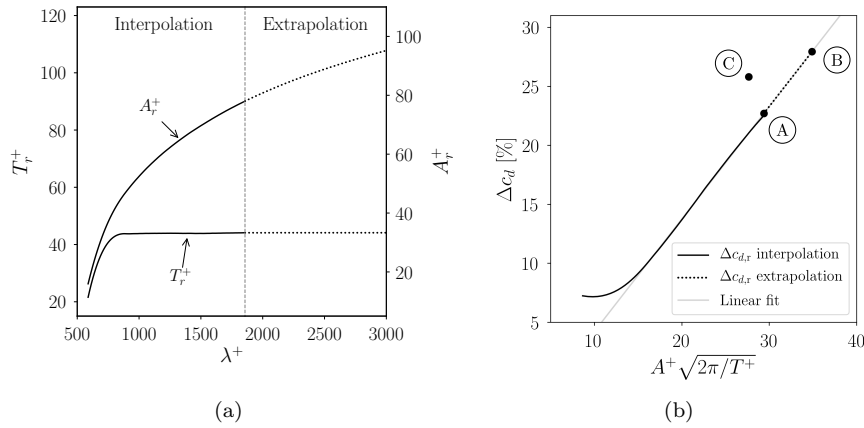


Fig. 8: (a) Projection of the ridgeline in the $\lambda^+ - T^+$ and $\lambda^+ - A^+$ planes. (b) Drag reduction along the ridgeline as a function of the scaling proposed by Tomiyama and Fukagata [48]. The solid circles marked A, B, and C correspond to the likewise marked points in Fig. 7.

a triple decomposition [18] of the flow variables is used

$$\phi = \underbrace{\bar{\phi} + \tilde{\phi}}_{\langle \phi \rangle} + \phi'', \quad (3)$$

where $\bar{\phi}$ is the temporal and spanwise average, $\tilde{\phi}$ are periodic fluctuations, $\langle \phi \rangle = \bar{\phi} + \tilde{\phi}$ are phase averaged quantities, and ϕ'' are stochastic fluctuations. Using this decomposition, $\bar{\phi} = f(x, y)$ represents phase independent quantities, $\tilde{\phi} = f(x, y, z)$ are the periodic fluctuations generated through the actuation, i.e., the secondary flow field, and $\phi'' = f(x, y, z, t)$ are turbulent fluctuations. Spanwise averages are obtained along lines of constant distance from the wall, i.e., along the curved mesh lines. This calculation of the spanwise average suffers from some uncertainty for short wavelengths with high amplitudes, where the traveling wave massively intrudes into the boundary layer. For spanwise averages of long wavelengths as in the N_{80} case, where the local perturbation of the viscous sublayer and the buffer layer is less drastic, this problem does not occur.

A first overall impression of the impact of the wave actuation on the turbulent coherent structures is given in Fig. 9 by comparing contours of the λ_2 -criterion [21] for the random velocity fluctuations u_i'' . It is evident that the total number of vortical structures in the near-wall region is significantly reduced for the actuated flow. Extended regions of little to hardly any structures occur in Fig. 9(b). A closer look evidences that unlike the structures of the non-actuated reference flow in Fig. 9(a), the structures of the actuated flow are inclined to the left and right depending on the phase angle of the traveling wave. It will be discussed in Sec. 4.6 that this wave determined orientation of the flow structures is an important feature related to drag reduction [49].

To highlight the influence of the actuation on the instantaneous flow field, Fig. 10 shows contours of the instantaneous random fluctuations of the velocity

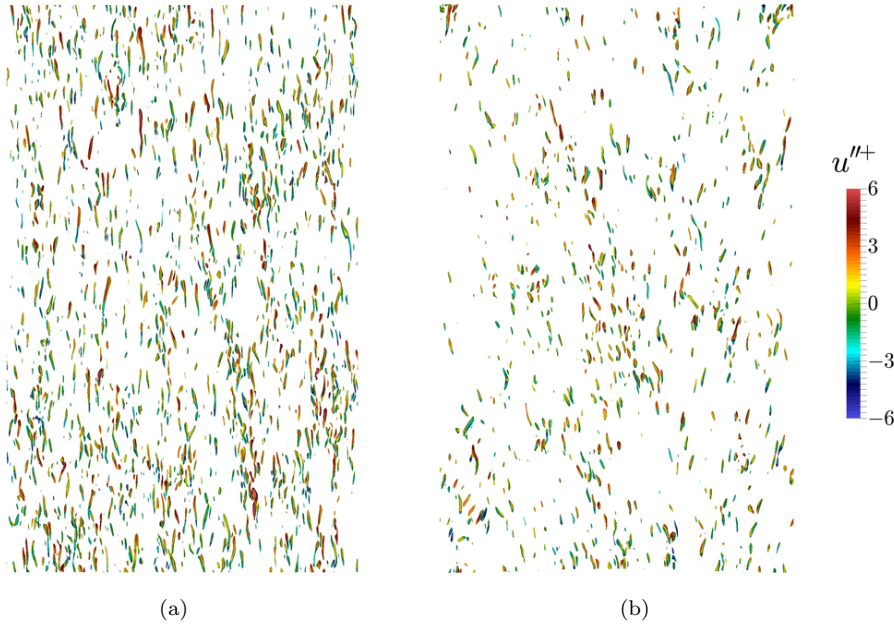


Fig. 9: Contours of the λ_2 -criterion [21] colored by the random velocity fluctuations u'' in the near-wall region $y^+ < 20$ of (a) the non-actuated reference case and (b) the actuated case with the highest drag reduction N_{80} , i.e., $\lambda^+ = 3000$, $T^+ = 50$, and $A^+ = 78$.

component in the streamwise direction u'' in a region $0 < y^+ < 20$ above the wall. For the non-actuated flow, regions of localized high-speed and low-speed fluid, i.e., streaks, are illustrated whose length and width are on the order of $\mathcal{O}(10^3)$ and $\mathcal{O}(10^2)$ in inner units. The actuated flow field shows much less pronounced regions of high- and low-speed fluid. That is, the distinctive structure of thin meandering streaks is considerably alleviated compared to the non-actuated reference case.

The wall-normal distributions of the phase averaged streamwise velocity $\langle u \rangle$ above the wave crest and in the wave trough and the mean velocity \bar{u} are shown in Fig. 11. The scaling with the friction velocity of the non-actuated reference case $u_{\tau,\text{ref}}$ in Fig. 11(a) illustrates the decrease of the velocity in the near-wall region. The wall-normal gradient at the wall is lowered, which results in drag reduction. Scaling the velocities with the friction velocity u_τ of the actuated wall in Fig. 11(b) leads to an offset of the velocity profiles in the logarithmic region with respect to the non-actuated reference case by $\Delta B^+ \approx 3.8$. Based on the idea of the analysis of the impact of roughness on fully turbulent flow [36, 8], Gatti and Quadrio [16] suggested the offset ΔB^+ to predict drag reduction at higher Reynolds numbers

$$\Delta B^+ = \sqrt{\frac{2}{c_{f,0}}} \left[(1 - \Delta c_f)^{-1/2} - 1 \right] - \frac{1}{\kappa} \left(\frac{\text{Re}_\tau}{\text{Re}_{\tau,0}} \right). \quad (4)$$

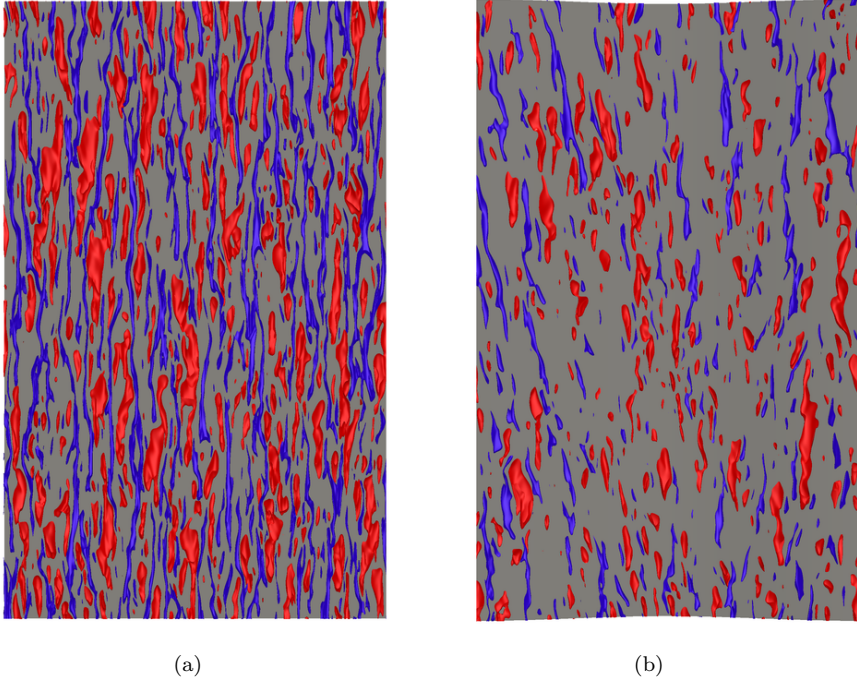


Fig. 10: Contours of the random streamwise velocity fluctuations for $u''^+ = -3$ (blue) and $u''^+ = 3$ (red) in the near-wall region $0 < y^+ < 20$ of (a) the non-actuated reference case and (b) the actuated case with the highest drag reduction N_{80} , i.e., $\lambda^+ = 3000$, $T^+ = 50$, and $A^+ = 78$.

Note, however, that this equation cannot be further simplified since for actuated turbulent boundary layer flow the term $\frac{\text{Re}_\tau}{\text{Re}_{\tau,0}}$ is neither constant, as for constant pressure gradient turbulent channel flow, nor can it be substituted by the drag reduction rate, as for constant flow rate turbulent channel flow. Thus, Δc_f cannot be directly determined by equation (4). Nevertheless, using the local values of $c_{f,0}$, Δc_f , Re_τ , and $\text{Re}_{\tau,0}$ at $x = 90\theta$ the calculated offset from equation (4) is $\Delta B^+ = 4.07$, which reasonably agrees with the result $\Delta B^+ = 3.8$ shown in Fig. 11(b). The velocity profiles in Fig. 11 show that for the current actuation neither the non-actuated nor the actuated friction velocity scaling—regardless from crest, trough, or spanwise averaged wall shear scaling—result in a collapsed distribution over the entire boundary layer. In other words, an inner scaling does not hold over the entire boundary layer.

Next, the components of the Reynolds stress tensor are depicted in Fig. 12. Through the actuation, the symmetric Reynolds stresses $\overline{u''_i u''_i}$ and the Reynolds shear stress $\overline{u'' v''}$ shown in Fig. 12(a) are significantly lowered with only minor phase variations. Considering all cases for $\lambda^+ > 1000$, a good correlation of the decrease of the skin-friction with the decrease of the peak of the streamwise velocity fluctuations is computed ($R = 0.90$). For the case N_{80} , the reductions at

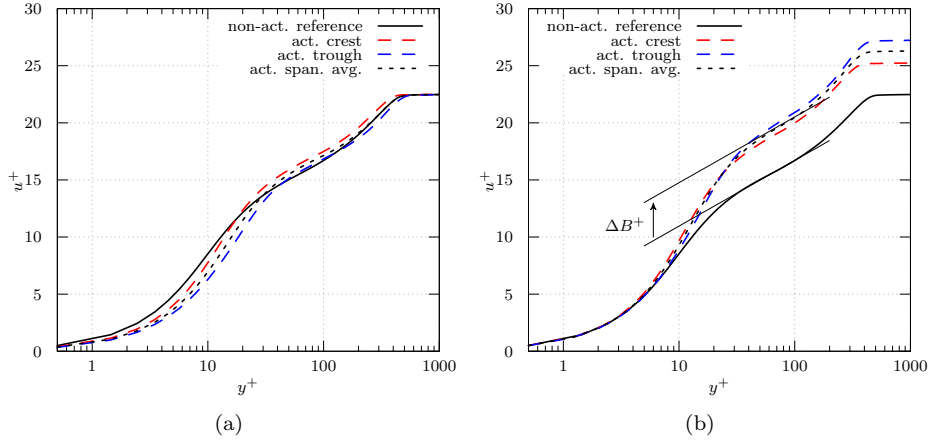


Fig. 11: Wall-normal distributions of the phase averaged streamwise velocity $\langle u \rangle$ above the crest and in the trough and the spanwise averaged mean velocity \bar{u} for the non-actuated reference case and the actuated case N_{80} , in (a) the N_{80} distributions are non-dimensionalized by the friction velocity of the non-actuated reference case and in (b) the N_{80} distributions are non-dimensionalized by the friction velocity of the actuated case N_{80} .

$y^+ = 14.2$, which defines the location of the peak of the streamwise fluctuations and the location of the maximum streamwise velocity streak intensity, are approx. 39% for the streamwise component and 62% for the shear-stress component. This suggests that the turbulent motion close to the wall is massively damped. Touber and Leschziner [49] have reported similarly large reductions in this region for spanwise wall oscillations without normal deflection. They emphasize the importance of the reduced near-wall Reynolds shear stress and drag, as characterized by the Fukagata, Iwamoto, Kasagi (FIK) identity [13], i.e., for the shear-stress contribution $c_{f,\text{RSS}} \sim \int_0^{\delta_{99}} (1-y)(-\overline{u''v''})dy$. The structural property of the turbulent motion is evidenced by the anisotropy invariant map [32] in Fig. 12(b). The stronger suppression of the streamwise fluctuations compared to the other components is illustrated by the shift of the actuated distribution away from one-dimensional turbulence in the upper right vertex to isotropic turbulence in the lower vertex.

The distributions of the joint probability density function (PDF) of the streamwise and the wall-normal stochastic velocity fluctuations u'' and v'' are presented in Fig. 13. High values in the upper left quadrant (negative u'' and positive v'') denote ejections of fluid from the near-wall region towards the outer flow, whereas high values in the lower right quadrant (positive u'' and negative v'') indicate sweeps of high-speed fluid from the outer flow towards the near-wall region. As can be seen in Fig. 13, an overall attenuation of the fluctuations is observed with a strong damping of the sweeps and ejections in the second and the fourth quadrant. Again, this is in agreement with the results from spanwise oscillating walls without normal deflection [1, 49].

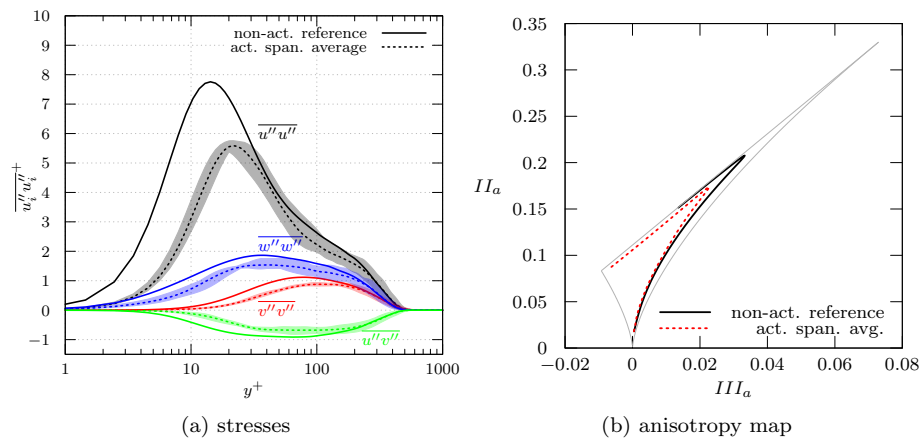


Fig. 12: Wall-normal distributions of the stochastic components of the Reynolds stress tensor scaled by the non-actuated reference friction velocity; (a) symmetric components $\overline{u''_i u''_i}$ and Reynolds shear stress $\overline{u''v''}$ for the non-actuated reference case and the actuated case N_{80} . Spanwise averaged values are shown as lines and the shaded regions illustrate phase variations of the depicted quantity; (b) Lumley anisotropy map of the Reynolds stress tensor.

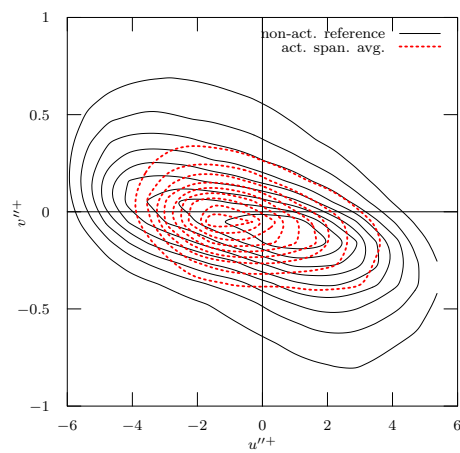


Fig. 13: Joint PDF of u'' and v'' at $y^+ = 12$ for the non-actuated reference case and the actuated case N_{80} .

Spanwise premultiplied energy spectra of the velocity fluctuations $\kappa E_{u''_i u''_i}$, where $\kappa = 2\pi/l_z$ is the wavenumber, are presented in Fig. 14. Each spectrum is normalized by the total resolved energy of the corresponding velocity component and the related case, i.e., the non-actuated reference case and N_{80} . No general decrease in the energy peak of the actuated case is observed, only a shift in the energy distribution as a function of the structural wavelength and wall-normal coordinate can be seen. A comparison between the two differently normalized spectra for the streamwise component (cf. Fig. 14(a) and Fig. 14(b)) shows an energy decrease especially for the small scales and in the near-wall region. In other words, for the actuated case N_{80} the energy is accumulated further off the wall in the larger scale turbulent structures. The peak of the non-actuated reference case at $\lambda^+ \approx 100$, which is associated with the typical spacing of the near-wall streaks of $l_z^+ = \mathcal{O}(100)$, becomes less pronounced for the actuated case N_{80} and is shifted off the wall. This observation corroborates the visual impression from Fig. 10 of a strong reduction of the near-wall streaks for the actuated case. Similar tendencies are observed for the wall-normal (cf. Fig. 14(c) and Fig. 14(d)) and the spanwise velocity component (cf. Fig. 14(e) and Fig. 14(f)). Additionally, a stronger concentration of the energy in the length scale range of the near-wall streaks is observed for the spanwise velocity component. There is a sharper peak for the actuated case in comparison to a broader energy distribution in the non-actuated case.

In Fig. 15 the phase averaged and spanwise averaged distributions of the vorticity fluctuations $\omega''_i \omega''_i$ are presented as a function of the wall-normal distance. The comparison of the profiles of each component shows that the major attenuation is observed in the wall-normal and the spanwise components, whereas the streamwise component shows only minor changes. Generally, for all cases with $\lambda^+ > 1000$ a good correlation between the decrease of the skin-friction and the decrease of the peak of the wall-normal ($R = 0.96$) and spanwise ($R = 0.98$) vorticity fluctuations was found. Again, similar vorticity trends were reported for spanwise oscillating walls [49]. The drag reduction was discussed to be caused by the weakening of velocity streaks near $y^+ \approx 10$ [1]. That is, at least for actuation with large wavelengths $\lambda^+ > 1000$, a direct interference with quasi-streamwise vortices [48] has a minor effect on drag reductions.

The comparison of the vorticity fluctuation contours for four cases, i.e., the non-actuated reference case, the case with the highest drag increase N_2 , a case with moderate drag reduction N_{24} , and the case with the highest drag reduction N_{80} , in Fig. 16 shows details about the phase dependence of the overall structure of the vorticity field. It is obvious that the drag increase is associated with strongly enlarged and highly phase dependent vorticity contours. Due to the high amplitude and short wavelength sinusoidal wall motion, the boundary layer flow is massively perturbed. This is completely different for the two drag reduction cases, where the overall boundary layer structure is maintained but with reduced values of the wall-normal and spanwise vorticity component. Phase variations occur especially for the wall-normal component with the highest decrease above the wave crest and the lowest decrease in the wave trough. Note, however, that despite the clear phase variations, the overall lowered vorticity levels are maintained throughout the entire actuation period, as shown in Fig. 15.

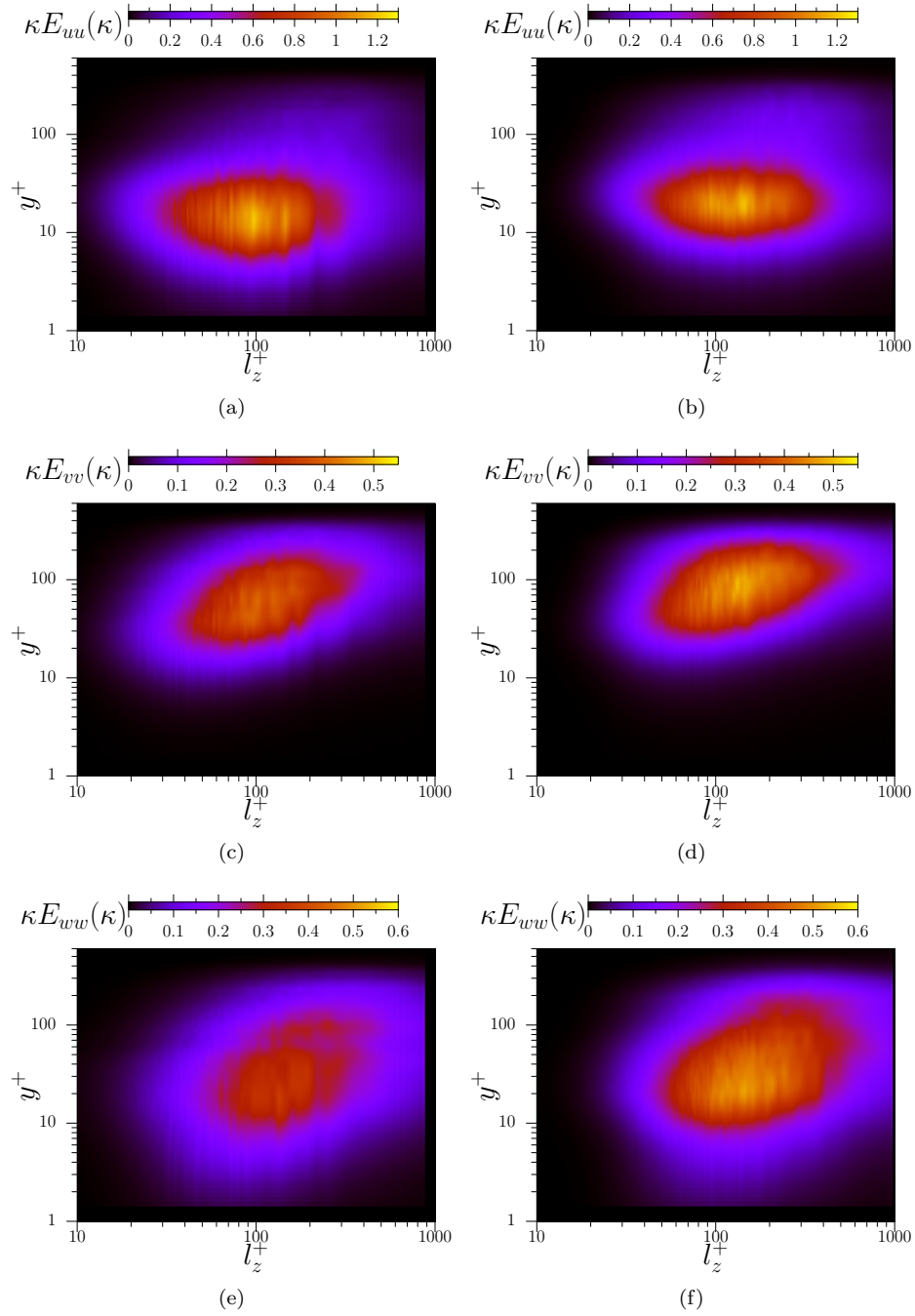


Fig. 14: Spanwise premultiplied energy spectra of the velocity fluctuations $u''_i u''_i$, normalized by the total resolved energy of the related component and the related case for (left) the non-actuated reference case and (right) the actuated case with the highest drag reduction N_{80} ; (a),(b) streamwise, (c),(d) wall-normal, and (e),(f) spanwise velocity component.

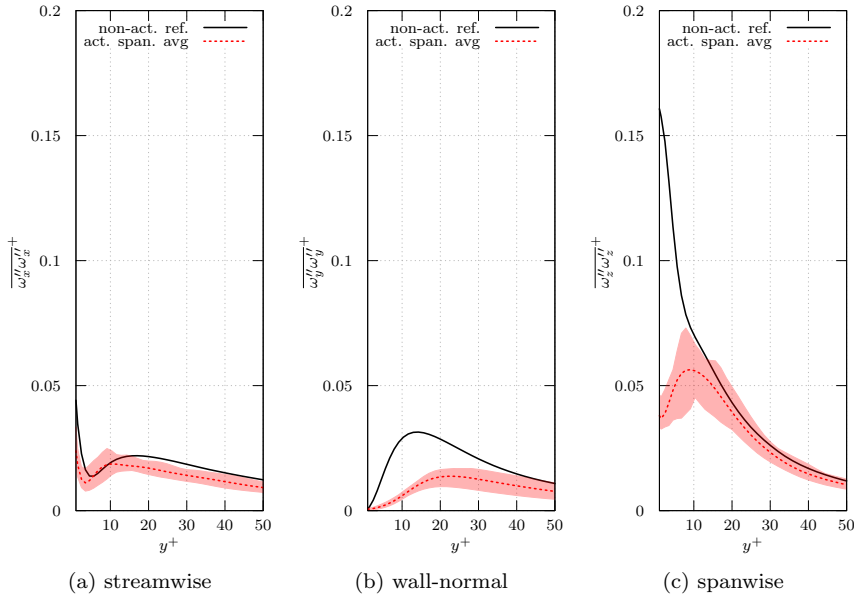


Fig. 15: Wall-normal distributions of the phase and spanwise averaged vorticity fluctuations $\overline{\omega''_i \omega''_i}$ for the non-actuated reference case and the actuated case N_{80} ; (a) streamwise, (b) wall-normal, and (c) spanwise component.

4.6 Spanwise shear

To investigate the secondary flow strength and its effect on the near-wall turbulent structures, the Stokes strain $\partial \tilde{w}^+ / \partial y^+$, i.e., the rate of change in the wall-normal direction of the periodic fluctuations of the spanwise velocity component, is considered in Fig. 17 for cases with wavelengths $\lambda^+ = 200$, $\lambda^+ = 1000$, $\lambda^+ = 1800$, and $\lambda^+ = 3000$. Based on the data summarized in Tab A1 in the appendix, for each $\lambda^+ = \text{const}$ set the cases with the highest, medium, and lowest skin-friction reduction are shown. The Stokes strain is used to characterize the Stokes layer that develops above an oscillating wall without any wall-normal deflection. However, similar to a configuration with pure spanwise oscillating walls [22, 49] a Stokes-like layer is also generated by a transversal wave motion of the surface. Through the introduction of a periodic wall-normal velocity \tilde{v} , a periodic spanwise velocity component \tilde{w} is induced via mass conservation resulting in a wall-normal shear distribution defining a Stokes layer. Cases with a high drag reduction generally show a high level of symmetric, i.e., positive and negative, spanwise shear very close to the wall, whereas less symmetric shear distributions yield lower drag reduction. When the Stokes drag significantly increases near the wall, i.e., a singular-like distribution occurs, the drag reduction reduces drastically. This observation supports the assumption that the drag reduction mechanism is strongly linked to spanwise oscillations which are generated either by wave oscillations [49], traveling waves

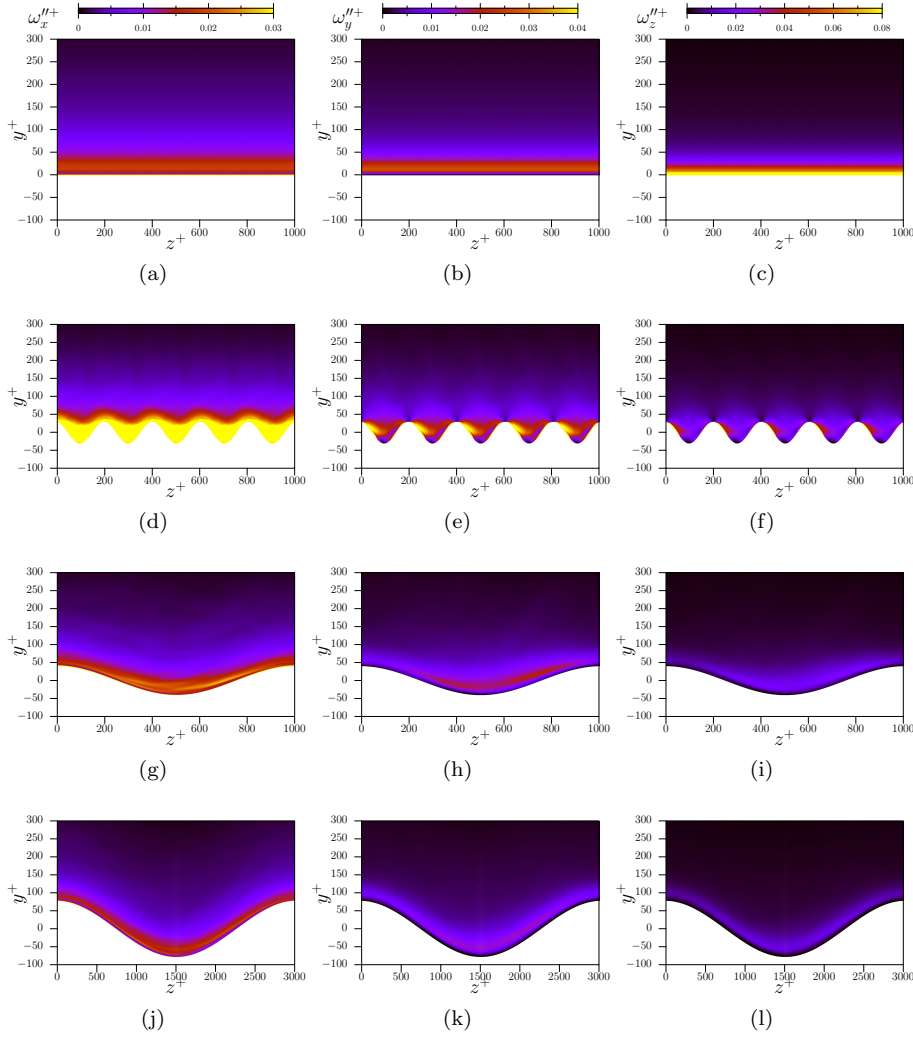


Fig. 16: Contours of the vorticity fluctuations $\overline{\omega_i''\omega_i''}$ in the y - z -plane at $x = 90\theta$ for (first row (a),(b),(c)) the non-actuated reference case, (second row (d),(e),(f)) the case with the highest drag increase N_2 , (third row (g),(h),(i)) a case with moderate drag reduction N_{24} , and (fourth row (j),(k),(l)) the case with the highest drag reduction N_{80} ; (left) streamwise, (center) wall-normal, and (right) spanwise vorticity component. Note that case N_{80} has a wavelength of $\lambda^+ = 3000$, the images for this case are thus compressed for lack of space.

of spanwise forcing [11], spanwise velocity at the wall [54], or spanwise transversal surface waves [25, 28].

The assumption of the importance of the oscillating spanwise shear for skin-friction reduction also yields an explanation for the increasing skin-friction reduction with growing wavelength, which agrees with an observation of Du et al. [11]. For short wavelengths, e.g., $\lambda^+ = 200$, the integration of the spanwise shear distribution over the spanwise width of a near-wall streak, i.e., $l_z^+ = \mathcal{O}(100)$, results in only a minor force in the spanwise direction acting on the streaks. For wavelengths $\lambda^+ > 1000$, however, the spanwise shear varies only slightly over the width of a streak, therefore a considerable spanwise force is determined by the integration over the spanwise streak width. Note that this behavior does not occur for spanwise wall oscillations, since the periodic spanwise shear does not depend on the spanwise coordinate.

A comparison of spanwise and streamwise shear is shown in Fig. 18. Touber and Leschziner [49] discuss a certain optimal scenario for oscillatory forcing in turbulent channel flow, where the ratio of spanwise to streamwise shear reaches values of up to $\frac{\partial \bar{w}^+ / \partial y^+}{\partial u^+ / \partial y^+} \approx 3$. Fig. 18(b) shows that a similar value of this ratio is obtained for the case with the highest skin-friction reduction N_{80} , whereas a lower ratio is obtained for the cases with medium (N_{82}) and low (N_{83}) skin-friction reduction. For all cases, the change of the skin-friction is well correlated, i.e., $R = 0.84$ at the wave crest and $R = 0.85$ in the wave trough, with a spanwise-to-streamwise shear ratio of $\frac{\partial \bar{w}^+ / \partial y^+}{\partial u^+ / \partial y^+} = 3.1$. Overall, the results for the spanwise traveling transversal waves in Fig. 17 underline the similarities to other drag reduction techniques based on periodic spanwise forcing. The results of the cases with lower wavelength in combination with high amplitude and high frequency deviate from this observation due to the increased wetted surface.

4.7 Energy saving analysis

The previous discussion has shown that considerable drag reduction rates have been obtained. However, drag reduction is not the only metric of interest. From a prospective application point of view, the question of net energy saving and its relation to drag reduction must be addressed. The ideal net energy saving is defined as

$$\Delta P_{\text{net}} = \frac{P_{d,\text{ref}} - (P_{d,\text{act}} + P_{\text{control}})}{P_{d,\text{ref}}} \cdot 100, \quad (5)$$

where $P_{d,\text{ref}/\text{act}} = u_\infty(F_f + F_p)$ is the power necessary to overcome the friction F_f and pressure forces F_p of the non-actuated $P_{d,\text{ref}}$ and actuated surface $P_{d,\text{act}}$ in the streamwise direction. The power spent on control P_{control} , i.e., on deflecting the surface for the traveling wave, is computed by

$$P_{\text{control}} = \int_{A_{\text{surf}}} v(x, z) (\tau_w \mathbf{e}_{xz} + p \mathbf{e}_y) \cdot \mathbf{n} dA, \quad (6)$$

where $\mathbf{e}_{xz} = (1, 0, 1)^T$ is a combination of the unit vectors in the streamwise and wall-normal direction. Hence, P_{control} is a combination of the viscous and pressure forces effective in the y -direction multiplied by the speed of the wall motion in the y -direction. The values of P_{control} and ΔP_{net} are depicted in Fig. 19 for all cases.

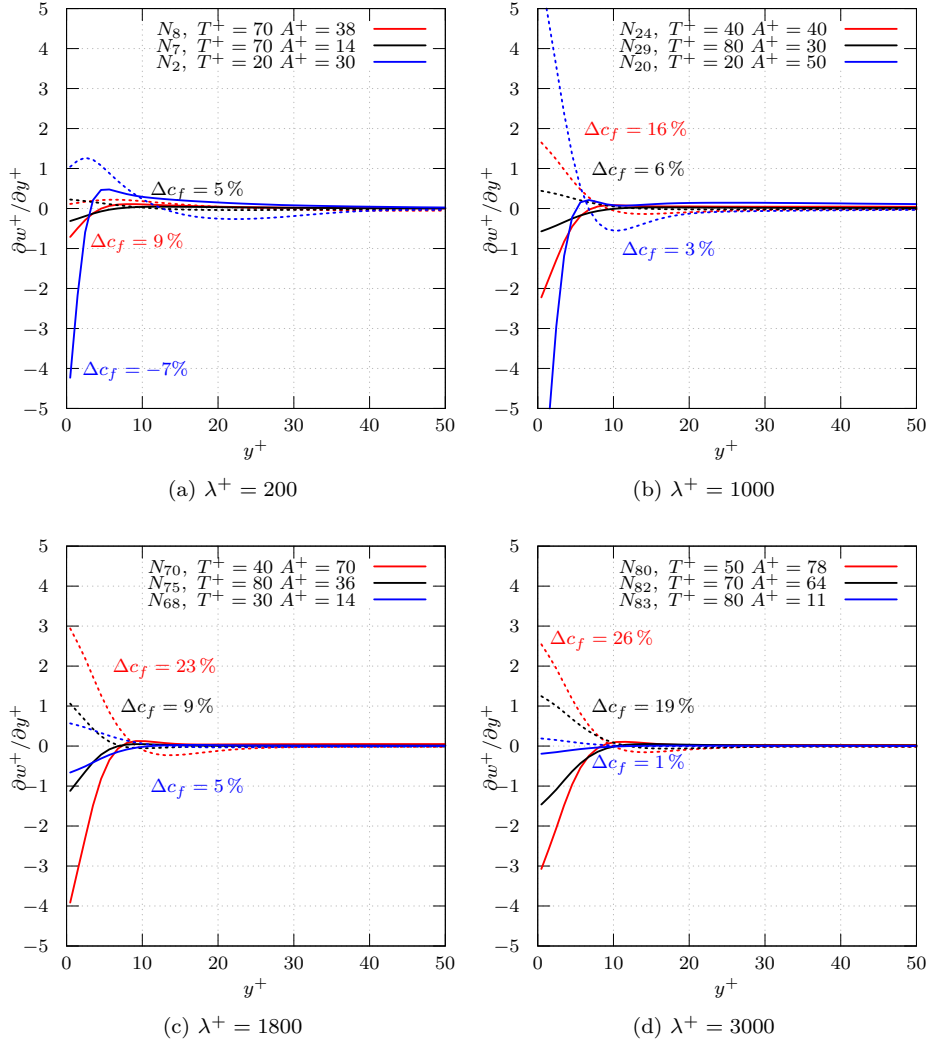


Fig. 17: Phase averaged spanwise shear above the wave crest (—) and in the wave trough (---) for wavelengths (a) $\lambda^+ = 200$, (b) $\lambda^+ = 1000$, (c) $\lambda^+ = 1800$, and (d) $\lambda^+ = 3000$. The cases listed in Tab. A1 in the appendix are representative for high (N_8 , N_{24} , N_{70} , N_{80}), medium (N_7 , N_{29} , N_{75} , N_{82}), and low (N_{20} , N_{68} , N_{83}) skin-friction reduction or skin-friction increase (N_2) at each wavelength.

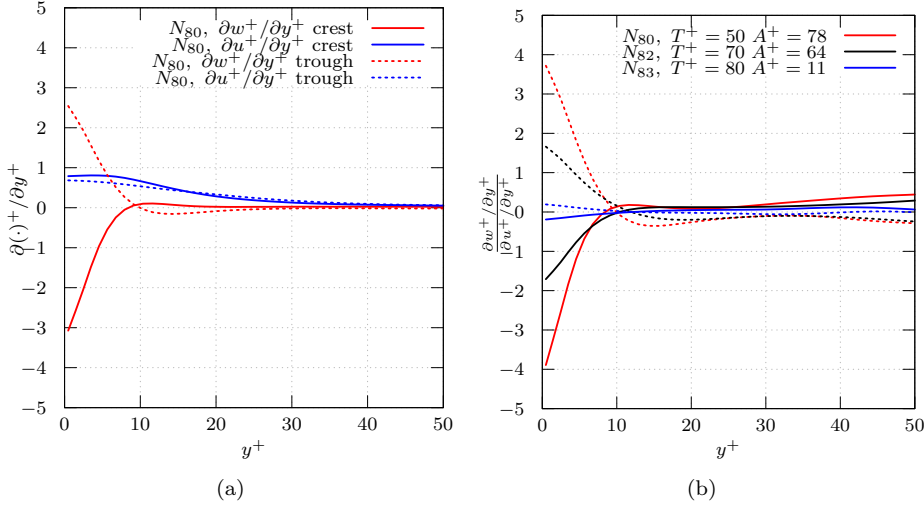


Fig. 18: Wall-normal distributions of (a) the phase averaged streamwise and spanwise shear for the actuated case N_{80} and (b) the ratio of the phase averaged spanwise and streamwise shear for cases with high (N_{80}), medium (N_{82}), and low (N_{83}) drag reduction.

The data for ΔP_{net} are also listed in Tab. A1 in the appendix. Fig. 19(a) shows the expected approximately linear dependence between the power spent P_{control} and the actuation velocity cubed $(V^+)^3 = (2\pi A^+/T^+)^3$.

It is evident from Fig. 19(b) that net power saving is only obtained for a few cases with a maximum of $\Delta P_{\text{net}} = 10\%$ for case N_{84} . Most cases clearly show no net power saving but net power loss. For instance, for N_{20} ΔP_{net} is $\Delta P_{\text{net}} = -289\%$, i.e., almost the fourfold $P_{d,\text{ref}}$ has to be invested.

A closer look at the net-power-saving cases in Fig. 19(c) shows that high drag reduction rates are no indicator for high net power saving. That is, there is no linear relation between drag reduction and net power saving. Instead, a high value of the scaling parameter $A^+ \sqrt{2\pi/T^+}$ obtained by a low amplitude speed $2\pi A^+/T^+$ leads to positive net power saving. Thus, as expected, there is a trade-off between the minimum power input to effectively influence the turbulent boundary layer and a maximum power input above which the energy costs grow tremendously. In the current parameter range, the optimum energy saving solution, i.e., $\Delta P_{\text{net}} = 10\%$, is achieved for the N_{84} case with $\lambda^+ = 3000$, $T^+ = 90$, and $A^+ = 66$, which possesses just a medium drag reduction of $\Delta c_d = 16\%$. Note that the parameters that result in high net energy saving are in the upper range of the interval. Furthermore, the data in Tab. A1 in the appendix indicates that the sensitivity of ΔP_{net} is less pronounced for larger wavelength and above a wave period of 60.

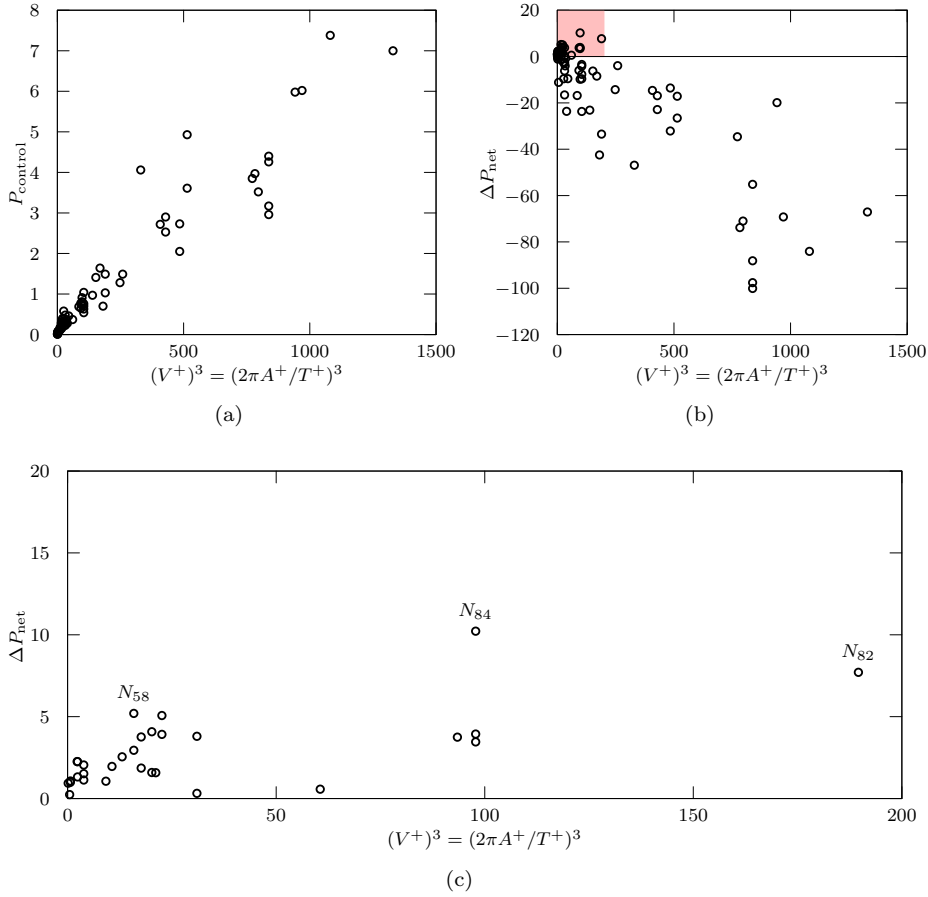


Fig. 19: Dependence of (a) the power spent P_{control} and (b) the net power saving ΔP_{net} on the cube of the actuation velocity amplitude $(V^+)^3 = (2\pi A^+/T^+)^3$; a zoom of the red rectangle in (b) is shown in (c). To indicate which cases possess net power saving the notation for three selected cases is given in (c).

5 Conclusions

To analyze drag reducing effects and the net energy saving potential of spanwise traveling transversal surface waves high-resolution large-eddy simulations were conducted. The parameter space defined by the wave amplitude, wave period, and wavelength was investigated based on 80 wave parameter setups for purely spanwise traveling waves. The variation of skin-friction reduction, i.e., mean wall-shear stress alteration, drag reduction, i.e., surface integrated wall-shear stress, and net energy saving was analyzed. In brief, a maximum drag reduction and net energy saving of 26 % and 10 % was found.

The highest skin-friction reduction was achieved for a period of $T^+ \approx 50$, which is lower than the one reported for spanwise oscillating wall and within the range of the streak formation time scale. Larger wavelengths and amplitudes yielded higher skin-friction reduction. For wavelengths larger than 1000 plus units, a scaling with the Stokes layer height and the velocity amplitude was found to predict skin-friction reduction reasonably well. Additionally, the difference between skin-friction reduction and drag reduction, i.e., the increase of the wetted surface was taken into account, was found to be substantial for short wavelengths in combination with high amplitudes. A drag-reduction model was derived from the sparse dataset using optimized support vector regression. From the model, a tendency to an asymptotic behavior of amplitude and period could be identified, supporting the assumption of an optimum period in the range $40 \leq T^+ \leq 50$ for large wavelengths. Moreover, a ridgeline behavior of optimum drag reduction in the high wavelength regime was extracted from the model.

The statistical results of the turbulent flow field confirmed this result for high wavelength configurations, where similar effects of the actuation on the near-wall region compared to spanwise oscillating walls were observed. That is, considerable reductions of the near-wall velocity streak strength were found for the cases with high drag reduction. For the highest drag reduction case, the smaller wall-shear stress was coupled to a substantial decrease of the Reynolds shear stress in the near-wall region. Generally, for large wavelength cases $\lambda^+ > 1000$ the decrease of the wall-normal and spanwise vorticity fluctuations strongly correlated with skin-friction reduction and drag reduction. A comparison among several configurations revealed that for unfavorable combinations of short wavelength and high amplitude, a considerable increase of the turbulent exchange resulting in skin-friction and drag increase was observed, whereas large wavelengths circumvented this effect and led to drag reduction. The periodic secondary flow field generated by the wavy surface motion approximated that of Stokes flow. Similar oscillating spanwise shear distributions were observed for many drag reducing cases, although no perfectly symmetrical oscillatory excitation of the near-wall structures is achieved.

No linear relationship between drag reduction and net energy saving was determined. That is, due to the non-linear response of the near-wall flow to the actuation the highest drag reduction does not result in the highest net energy saving. The maximum net energy saving $\Delta P_{\text{net}} = 10\%$ was achieved for a drag reduction of $\Delta c_d = 16\%$, which is clearly lower than the maximum drag reduction of $\Delta c_d = 26\%$. A high value of the product of the actuation amplitude speed and the thickness of the Stokes layer at low amplitude speed results in positive net energy saving. The susceptibility of ΔP_{net} is less pronounced for larger wavelength, which is a promising observation for prospective applications.

Acknowledgements

The research was funded by the Deutsche Forschungsgemeinschaft (DFG) in the framework of the research projects SCHR 309/52 and SCHR 309/68. The authors gratefully acknowledge the Gauss Centre for Supercomputing e.V. (www.gauss-centre.eu) for funding this project by providing computing time on the GCS Supercomputers Hazelhen at HLRS Stuttgart and JURECA at Jülich Supercomput-

ing Centre (JSC). BRN acknowledges support from the French National Research Agency (ANR) under grant ANR-17-ASTR-0022 (FlowCon).

Compliance with Ethical Standards

Conflict of Interests

The authors declare that they have no conflicts of interest.

A Appendix

N	L_z^+	λ^+	T^+	A^+	Δc_d [%]	Δc_f [%]	ΔA_{surf} [%]	ΔP [%]
1	1000	0	0	0	0	0	0.0	0
2	1000	200	20	30	-27	-7	19.4	-100
3	1000	200	30	21	-1	8	10.1	-17
4	1000	200	40	30	-9	9	19.4	-24
5	1000	200	50	45	-26	9	39.0	-42
6	1000	200	60	30	-10	8	19.4	-17
7	1000	200	70	14	0	5	4.7	-1
8	1000	200	70	38	-17	9	29.4	-24
9	1000	200	100	28	-9	7	17.2	-11
10	1000	500	20	30	0	4	3.5	-98
11	1000	500	30	22	9	10	1.9	-10
12	1000	500	40	21	8	9	1.7	-1
13	1000	500	40	30	8	11	3.5	-10
14	1000	500	60	30	5	8	3.5	-2
15	1000	500	70	36	3	8	4.9	-4
16	1000	500	70	64	-10	4	14.6	-33
17	1000	500	100	48	-3	5	8.6	-10
18	1000	1000	20	10	5	5	0.1	-6
19	1000	1000	20	30	13	13	0.9	-88
20	1000	1000	20	50	0	3	2.4	-289
21	1000	1000	40	10	3	3	0.1	1
22	1000	1000	40	20	7	8	0.4	0
23	1000	1000	40	30	12	13	0.9	-4
24	1000	1000	40	40	15	16	1.6	-14
25	1000	1000	40	50	15	17	2.4	-32
26	1000	1000	40	60	13	16	3.5	-55
27	1000	1000	80	10	1	1	0.1	0
28	1000	1000	80	20	3	4	0.4	2
29	1000	1000	80	30	6	6	0.9	3
30	1000	1000	80	40	9	10	1.6	4
31	1000	1000	80	50	9	11	2.4	1
32	1000	1000	80	60	9	12	3.5	-3
33	1000	1000	120	10	1	1	0.1	1
34	1000	1000	120	20	0	1	0.4	0
35	1000	1000	120	30	3	4	0.9	2
36	1000	1000	120	40	3	5	1.6	1
37	1000	1000	120	50	2	5	2.4	-1
38	1000	1000	120	60	2	6	3.5	-3

N	L_z^+	λ^+	T^+	A^+	Δc_d [%]	Δc_f [%]	ΔA_{surf} [%]	ΔP [%]
39	1200	0	0	0	0	0	0.0	0
40	1200	600	30	44	2	7	5.1	-74
41	1200	600	40	59	-4	5	8.9	-71
42	1200	600	50	36	9	12	3.5	-6
43	1200	600	60	21	5	6	1.2	2
44	1200	600	70	29	6	8	2.3	2
45	1200	600	80	66	-5	6	11.0	-23
46	1200	600	90	51	-1	6	6.8	-10
47	1200	600	100	14	2	2	0.5	1
N	L_z^+	λ^+	T^+	A^+	Δc_d [%]	Δc_f [%]	ΔA_{surf} [%]	ΔP [%]
48	1600	0	0	0	0	0	0.0	0
49	1600	1600	20	22	11	11	0.2	-47
50	1600	1600	40	34	14	14	0.4	-6
51	1600	1600	40	48	19	19	0.9	-23
52	1600	1600	50	60	19	20	1.4	-17
53	1600	1600	50	73	21	22	2.0	-35
54	1600	1600	60	27	8	8	0.3	4
55	1600	1600	70	71	17	19	1.9	-4
56	1600	1600	80	17	2	2	0.1	1
57	1600	1600	90	65	13	14	1.6	4
58	1600	1600	100	40	8	8	0.6	5
N	L_z^+	λ^+	T^+	A^+	Δc_d [%]	Δc_f [%]	ΔA_{surf} [%]	ΔP [%]
59	1800	0	0	0	0	0	0.0	0
60	1800	900	30	49	10	12	2.9	-84
61	1800	900	40	63	7	12	4.7	-69
62	1800	900	50	22	7	7	0.6	2
63	1800	900	50	44	12	14	2.3	-8
64	1800	900	70	28	7	8	0.9	3
65	1800	900	80	17	3	4	0.4	2
66	1800	900	80	60	6	9	4.3	-8
67	1800	900	90	39	6	7	1.8	2
68	1800	1800	30	14	5	5	0.1	-2
69	1800	1800	40	51	19	20	0.8	-27
70	1800	1800	40	70	22	23	1.5	-67
71	1800	1800	50	59	20	21	1.1	-15
72	1800	1800	60	44	15	15	0.6	3
73	1800	1800	60	75	21	22	1.7	-14
74	1800	1800	70	29	7	7	0.3	4
75	1800	1800	80	36	9	9	0.4	5
76	1800	1800	90	66	13	14	1.3	4
77	1800	1800	100	21	3	3	0.1	2
N	L_z^+	λ^+	T^+	A^+	Δc_d [%]	Δc_f [%]	ΔA_{surf} [%]	ΔP [%]
78	3000	0	0	0	0	0	0.0	0
79	3000	3000	40	51	21	21	0.3	-17
80	3000	3000	50	78	26	26	0.7	-20
81	3000	3000	60	26	7	7	0.1	4
82	3000	3000	70	64	19	19	0.4	8
83	3000	3000	80	11	1	1	0.0	1
84	3000	3000	90	66	16	16	0.5	10

Table A1: Actuation parameters of the turbulent boundary layer simulations, where each setup is denoted by a case number N . The quantity λ^+ is the spanwise wavelength of the traveling wave, T^+ is the period, and A^+ is the amplitude, all given in inner units, i.e., non-dimensionalized with the kinematic viscosity ν and the friction velocity u_τ . Each block includes setups with varying period and amplitude for a constant wavelength. The list includes the values of the averaged relative drag reduction Δc_d , the averaged relative skin friction reduction Δc_f , the relative increase of the wetted surface ΔA_{surf} , and the net power saving ΔP .

References

1. Agostini, L., Toubert, E., Leschziner, M.A.: Spanwise oscillatory wall motion in channel flow: drag-reduction mechanisms inferred from DNS-predicted phase-wise property variations at $Re_\tau = 1000$. *J. Fluid Mech.* **743**, 606–635 (2014)
2. Albers, M., Meysonnat, P.S., Schröder, W.: Actively reduced airfoil drag by transversal surface waves. *Flow Turbul. Combust.* **102**(4), 865–886 (2019)
3. Alkishriwi, N., Meinke, M., Schröder, W.: A large-eddy simulation method for low Mach number flows using preconditioning and multigrid. *Comp. Fluids* **35**(10), 1126–1136 (2006)
4. Bechert, D.W., Hoppe, G., Reif, W.E.: On the drag reduction of the shark skin. AIAA Paper No. 85-0546 (1985)
5. Boris, J.P., Grinstein, F.F., Oran, E.S., Kolbe, R.L.: New insights into large eddy simulation. *Fluid Dyn. Res.* **10**(4-6), 199–228 (1992)
6. Choi, K.S., Debisschop, J.R., Clayton, B.R.: Turbulent boundary-layer control by means of spanwise-wall oscillation. *AIAA Journal* **36**(7), 1157–1163 (1998)
7. Choi, K.S., Yang, X., Clayton, B.R., Glover, E.J., Atlar, M., Semenov, B.N., Kulik, V.M.: Turbulent drag reduction using compliant surfaces. *Proc. R. Soc. London, Ser. A* **453**(1965), 2229–2240 (1997)
8. Clauser, F.H.: The turbulent boundary layer. pp. 1–51. Elsevier (1956)
9. Cortes, C., Vapnik, V.: Support-vector networks. *Machine learning* **20**(3), 273–297 (1995)
10. Du, Y., Karniadakis, G.E.: Suppressing wall turbulence by means of a transverse traveling wave. *Science* **288**(5469), 1230–1234 (2000)
11. Du, Y., Symeonidis, V., Karniadakis, G.E.: Drag reduction in wall-bounded turbulence via a transverse travelling wave. *J. Fluid Mech.* **457**, 1–34 (2002)
12. Fernex, D., Semann, R., Albers, M., Meysonnat, P.S., Schröder, W., Noack, B.R.: Self-similar drag reduction formula from sparse data—optimization of turbulent skin-friction via spanwise travelling surface waves. *J. Fluid Mech.* In preparation. The preprint will be made available in *arXiv*. (2019)
13. Fukagata, K., Iwamoto, K., Kasagi, N.: Contribution of Reynolds stress distribution to the skin friction in wall-bounded flows. *Phys. Fluids* **14**(11), L73–L76 (2002)
14. García-Mayoral, R., Jiménez, J.: Drag reduction by riblets. *Philos. Trans. R. Soc. London, Ser. A* **369**(1940), 1412–1427 (2011)
15. García-Mayoral, R., Jiménez, J.: Hydrodynamic stability and breakdown of the viscous regime over riblets. *J. Fluid Mech.* **678**, 317–347 (2011)
16. Gatti, D., Quadrio, M.: Reynolds-number dependence of turbulent skin-friction drag reduction induced by spanwise forcing. *J. Fluid Mech.* **802**, 553–582 (2016)
17. Hirt, C.W., Amsden, A.A., Cook, J.L.: An arbitrary Lagrangian–Eulerian computing method for all flow speeds. *J. Comput. Phys.* **14**, 227–253 (1974)
18. Hussain, A.K.M.F., Reynolds, W.C.: The mechanics of an organized wave in turbulent shear flow. *J. Fluid Mech.* **41**(2), 241–258 (1970)
19. Ishaq, R., Kaiser, E., Morzyński, M., Fernex, D., Semaan, R., Albers, M., Meysonnat, P.S., Schröder, W., Noack, B.R.: Metric for attractor overlap. *J. Fluid Mech.* **874**, 720–755 (2019)
20. Itoh, M., Tamano, S., Yokota, K., Taniguchi, S.: Drag reduction in a turbulent boundary layer on a flexible sheet undergoing a spanwise traveling wave motion. *J. Turbul.* **7**, N27 (2006)
21. Jeong, J., Hussain, F.: On the identification of a vortex. *J. Fluid Mech.* **285**, 69–94 (1995)
22. Jung, W.J., Mangiavacchi, N., Akhavan, R.: Suppression of turbulence in wallbounded flows by highfrequency spanwise oscillations. *Phys. Fluids A* **4**(8), 1605–1607 (1992)
23. Kim, E., Choi, H.: Space-time characteristics of a compliant wall in a turbulent channel flow. *J. Fluid Mech.* **756**, 30–53 (2014)
24. Klumpp, S., Meinke, M., Schröder, W.: Numerical simulation of riblet controlled spatial transition in a zero-pressure-gradient boundary layer. *Flow Turbul. Combust.* **85**(1), 57–71 (2010a)
25. Klumpp, S., Meinke, M., Schröder, W.: Drag reduction by spanwise transversal surface waves. *J. Turbul.* **11** (2010b)
26. Klumpp, S., Meinke, M., Schröder, W.: Friction drag variation via spanwise transversal surface waves. *Flow Turbul. Combust.* **87**(1), 33–53 (2011)
27. Koh, S.R., Meysonnat, P., Meinke, M., Schröder, W.: Drag reduction via spanwise transversal surface waves at high Reynolds numbers. *Flow Turbul. Combust.* **95**(1), 169–190 (2015)

28. Koh, S.R., Meysonnat, P., Statnikov, V., Meinke, M., Schröder, W.: Dependence of turbulent wall-shear stress on the amplitude of spanwise transversal surface waves. *Comput. Fluids* **119**, 261–275 (2015)
29. Lardeau, S., Leschziner, M.A.: The streamwise drag-reduction response of a boundary layer subjected to a sudden imposition of transverse oscillatory wall motion. *Phys. Fluids* **25**(7), 075109 (2013)
30. Li, W., Roggenkamp, D., Hecken, T., Jessen, W., Klaas, M., Schröder, W.: Parametric investigation of friction drag reduction in turbulent flow over a flexible wall undergoing spanwise transversal traveling waves. *Exp. Fluids* **59**(6), 105 (2018)
31. Luhar, M., Sharma, A., McKeon, B.: A framework for studying the effect of compliant surfaces on wall turbulence. *J. Fluid Mech.* **768**, 415–441 (2015)
32. Lumley, J.L., Newman, G.R.: The return to isotropy of homogeneous turbulence. *J. Fluid Mech.* **82**(01), 161–178 (1977)
33. Meinke, M., Schröder, W., Krause, E., Rister, T.: A comparison of second- and sixth-order methods for large-eddy simulations. *Comput. Fluids* **31**(4), 695–718 (2002)
34. Meysonnat, P.S., Roggenkamp, D., Li, W., Roidl, B., Schröder, W.: Experimental and numerical investigation of transversal traveling surface waves for drag reduction. *Eur. J. Mech. B. Fluids* **55**, 313–323 (2016)
35. Moin, P., Shih, T., Driver, D., Mansour, N.N.: Direct numerical simulation of a three-dimensional turbulent boundary layer. *Phys. Fluids A* **2**(10), 1846–1853 (1990)
36. Nikuradse, J.: Strömungsgesetze in rauhen Röhren. *VDI-Forschungsheft* **361** (1933)
37. Quadrio, M.: Drag reduction in turbulent boundary layers by in-plane wall motion. *Philos. Trans. R. Soc. London, Ser. A* **369**(1940), 1428–1442 (2011)
38. Quadrio, M., Ricco, P.: Critical assessment of turbulent drag reduction through spanwise wall oscillations. *J. Fluid Mech.* **521**, 251–271 (2004)
39. Renze, P., Schröder, W., Meinke, M.: Large-eddy simulation of film cooling flows at density gradients. *Int. J. Heat Fluid Flow* **29**(1), 18–34 (2008)
40. Ricco, P.: Modification of near-wall turbulence due to spanwise wall oscillations. *J. Turbul.* **5**, N24 (2004)
41. Ricco, P., Wu, S.: On the effects of lateral wall oscillations on a turbulent boundary layer. *Exp. Therm Fluid Sci.* **29**(1), 41–52 (2004)
42. Roidl, B., Meinke, M., Schröder, W.: A reformulated synthetic turbulence generation method for a zonal RANS–LES method and its application to zero-pressure gradient boundary layers. *Int. J. Heat Fluid Flow* **44**, 28–40 (2013)
43. Rütten, F., Schröder, W., Meinke, M.: Large-eddy simulation of low frequency oscillations of the Dean vortices in turbulent pipe bend flows. *Phys. Fluids* **17**(3), 035107 (2005)
44. Schlatter, P., Örlü, R.: Assessment of direct numerical simulation data of turbulent boundary layers. *J. Fluid Mech.* **659**, 116–126 (2010)
45. Spalart, P.R., McLean, J.D.: Drag reduction: enticing turbulence, and then an industry. *Philos. Trans. R. Soc. London, Ser. A* **369**(1940), 1556–1569 (2011)
46. Statnikov, V., Meinke, M., Schröder, W.: Reduced-order analysis of buffet flow of space launchers. *J. Fluid Mech.* **815**, 1–25 (2017)
47. Tamano, S., Itoh, M.: Drag reduction in turbulent boundary layers by spanwise traveling waves with wall deformation. *J. Turbul.* **13**, N9 (2012)
48. Tomiyama, N., Fukagata, K.: Direct numerical simulation of drag reduction in a turbulent channel flow using spanwise traveling wave-like wall deformation. *Phys. Fluids* **25**(10), 105115 (2013)
49. Touber, E., Leschziner, M.A.: Near-wall streak modification by spanwise oscillatory wall motion and drag-reduction mechanisms. *J. Fluid Mech.* **693**, 150–200 (2012)
50. Walsh, M., Weinstein, L.: Drag and heat transfer on surfaces with small longitudinal fins. In: *11th Fluid and Plasma Dynamics Conference*, p. 1161 (1978)
51. Walsh, M.J., Sellers III, W.L., Mcginley, C.B.: Riblet drag at flight conditions. *J. Aircraft* **26**(6), 570–575 (1989)
52. Yudhistira, I., Skote, M.: Direct numerical simulation of a turbulent boundary layer over an oscillating wall. *J. Turbul.* **12**, N9 (2011)
53. Zhang, C., Wang, J., Blake, W., Katz, J.: Deformation of a compliant wall in a turbulent channel flow. *J. Fluid Mech.* **823**, 345–390 (2017)
54. Zhao, H., Wu, J.Z., Luo, J.S.: Turbulent drag reduction by traveling wave of flexible wall. *Fluid Dyn. Res.* **34**(3), 175–198 (2004)